Rapid Communications

Role of virtual band population for high harmonic generation in solids

Yasuyuki Sanari,[1] Hideki Hirori,[1,*] Tomoko Aharen,[1] Hirokazu Tahara,[1] Yasushi Shinohara,[2,3] Kenichi L. Ishikawa,[2,3,4] Tomohito Otobe,[5] Peiyu Xia,[6] Nobuhisa Ishii,[6] Jiro Itatani,[6] Shunsuke A. Sato,[7,8] and Yoshihiko Kanemitsu[1,*]

[1]*Institute for Chemical Research, Kyoto University, Uji, Kyoto 611-0011, Japan*
[2]*Photon Science Center, Graduate School of Engineering, The University of Tokyo, Bunkyo-ku, Tokyo 113-8656, Japan*
[3]*Department of Nuclear Engineering and Management, Graduate School of Engineering, The University of Tokyo, Bunkyo-ku, Tokyo 113-8656, Japan*
[4]*Research Institute for Photon Science and Laser Technology, The University of Tokyo, 7-3-1 Hongo, Bunkyo-ku, Tokyo 113-0033, Japan*
[5]*Kansai Photon Science Institute, National Institutes for Quantum and Radiological Science and Technology, Kizugawa, Kyoto 619-0615, Japan*
[6]*Institute for Solid State Physics, The University of Tokyo, Kashiwa, Chiba 277-8581, Japan*
[7]*Center for Computational Sciences, University of Tsukuba, Tsukuba 305-8577, Japan*
[8]*Max Planck Institute for the Structure and Dynamics of Matter, Luruper Chaussee 149, 22761 Hamburg, Germany*

(Received 23 October 2019; revised 1 May 2020; accepted 13 July 2020; published 30 July 2020)

We study the sub-band-gap high harmonic generation (HHG) in a methylammonium lead trichloride single crystal. Anisotropy in the crystal orientation dependence of the high harmonic yield is observed, and the yield varies substantially with the electric field strength of the midinfrared laser pulse used for excitation. Our real-time *ab initio* simulations reproduce the experimental results well and also show that the HHG is independent of the interband decoherence time. Based on a microscopic analysis of the intraband current, we reveal that the orientation dependence of the HHG in this perovskite semiconductor is governed by the virtual band population, rather than the anharmonicity of the electronic band structure.

DOI: 10.1103/PhysRevB.102.041125

Extremely nonlinear optical processes are quite different from those in the linear (perturbative) regime and are considered to be important for new fields of study and applications [1,2]. In particular, the recent demonstration of high harmonic generation (HHG) in solids is expected to lead to new approaches to attosecond photonics and coherent extreme ultraviolet (XUV) sources [3–11]. Here, the HHG is induced by strong interactions between intense laser fields and matter. While the HHG in gases has already found its way into applied science [1,2], the mechanism of HHG in solids has been intensively discussed in order to understand the fundamentals that are required for applications such as band reconstruction methodologies in addition to coherent sources.

HHG in solids can be categorized as harmonics generated via interband or intraband processes. Both processes take place after the excitation of carriers induced by tunneling ionization [11]. To describe the nonlinear current in the system, we introduce the time-dependent current $J(t)$. A simple expression of the intraband current is $J_{\mathrm{intra}}(t) = e\Delta n V(t)$ [3,5,9,11], where e, Δn, and V denote the elementary charge, the population change, and velocity, respectively. Note that the intraband process is expected to be significant in the case of sub-band-gap HHG [12,13]. In this case, the Fourier transform of $J_{\mathrm{intra}}(t)$ corresponds to the HHG spectrum, and the latter allows us to investigate the band structure even in regions where the effective mass approximation is not valid. Thus, the crystallographic dependence of the high-order harmonic (HH) yield reflecting the band structure has been studied intensively [12–15]. Two fundamental results for HHG are as follows: The band population changes coherently during nonresonant excitation [16–19], and the ionization processes, i.e., real/virtual excitations, are essential to understand nonlinear optical processes [20–23]. However, work that explicitly analyzes the influences of virtual excitation on HHG in solids is lacking. A better understanding of the roles of both velocity anisotropies and of population changes in HHG should be useful for progress in applications such as nonlinear optical device design and band reconstruction methodologies.

In this Rapid Communication, we studied the crystal orientation dependence of the HH yield from a methylammonium lead trichloride ($MAPbCl_3$) single crystal (thickness 0.3 mm). We also recorded the HH yields as a function of the electric field for several harmonic orders. *Ab initio* simulations were performed to analyze the results. The good agreement between the experiment and calculation shows that the virtual band population (rather than the anharmonic potential in the band structure) governs the orientation dependence of HHG.

The $MAPbCl_3$ perovskite semiconductor possesses a cubic structure at room temperature as shown in Fig. 1(a). This material is a good candidate for an HHG source with a wide spectral range, because of its good transparency in the entire visible region (as a result of the large band-gap energy of $E_g = 3.15$ eV) [24–26]. Besides the technological importance of this solution processable material [27–31], its high directionality of the chemical bond between the metallic cation

*Corresponding authors: hirori@scl.kyoto-u.ac.jp; kanemitu@scl.kyoto-u.ac.jp

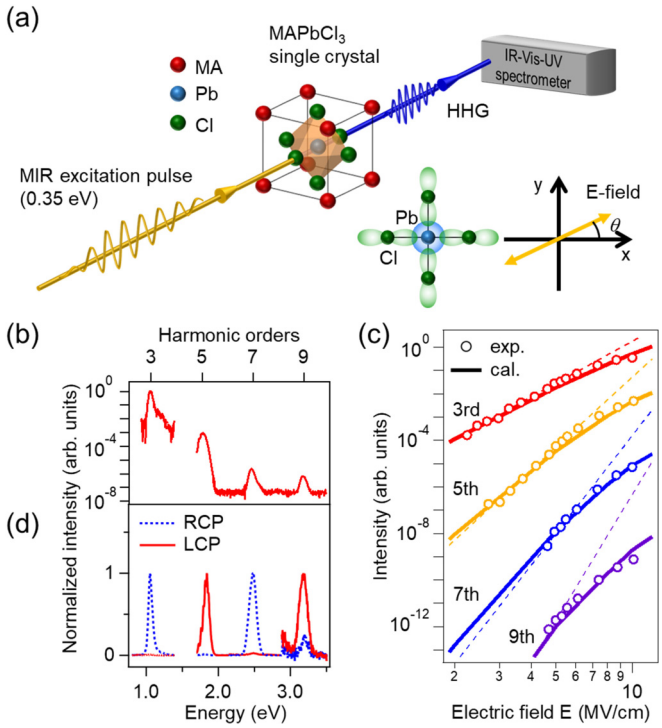

FIG. 1. (a) Schematics of experimental setup for HHG measurement and the perovskite ABX_3 crystal structure where $A = CH_3NH_3^+$ (MA), $B =$ Pb, and $X =$ Cl. The schematic atomic arrangement next to the ABX_3 crystal structure illustrates the electron wave functions of the Cl $3p$ (light green) and Pb $6s$ orbitals (light blue). The yellow arrow shows how we define the direction of the fundamental excitation field. (b) HHG spectra of a bulk $MAPbCl_3$ single crystal for $E = 10\,\mathrm{MV/cm}$. (c) Measured (open circles) and calculated (solid lines) harmonic yields as a function of the peak electric field E inside the sample for harmonic orders $h = 3, 5, 7$, and 9. The dashed lines are proportional to E^{2h} and serve as guides for the eye. (d) Right-handed circularly polarized (RCP) and left-handed circularly polarized (LCP) components of the HHG spectrum under LCP excitation (blue dashed and red solid lines, respectively). The data are offset for clarity.

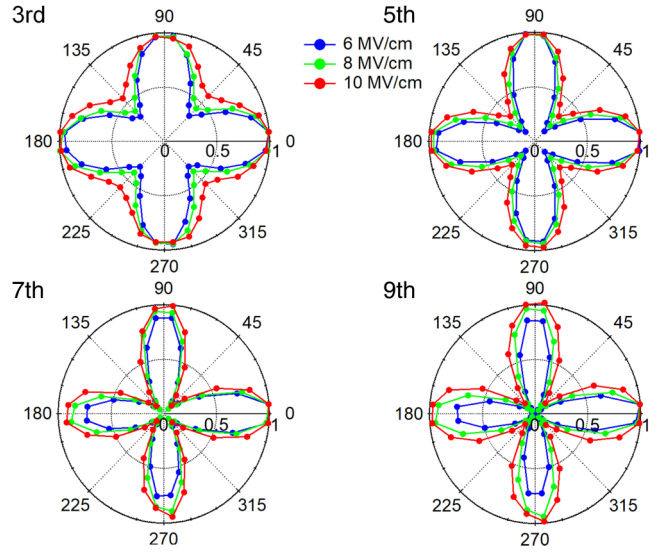

FIG. 2. Measured θ dependences of HH yields obtained for $E = 6$, 8, and 10 MV/cm (shown with blue, green, and red lines, respectively). The harmonic orders are indicated on the left upper corners of each data set and the maximum peak intensities are normalized.

(Pb) and the halide anion (Cl) can cause a highly anisotropic nonlinear absorption [32,33]. This is beneficial for examining how HHG is actually related to the nonlinearity of the laser-induced current.

A high-quality single crystal with a large size was synthesized using an antisolvent vapor-assisted crystallization technique [see Supplemental Material (SM) Secs. I and II [34]). Figure 1(b) plots the HH emission spectrum obtained from the sample under excitation with a linearly polarized midinfrared (MIR) pulse. The center energy of the 60-fs MIR pulse was $\hbar\omega_0 = 0.35\,\mathrm{eV}$ (corresponding to a wavelength of 3.5 μm) and the maximum peak electric field E was 10 MV/cm. To obtain these data, the laser electric field vector was aligned with the chemical bond direction between Cl and Pb ions [x axis in Fig. 1(a)], corresponding to $\theta = 0°$. The spectra extend from the visible to the ultraviolet region up to the ninth order as indicated on the upper side of Fig. 1(b) and show only odd harmonics; the absence of even harmonics originates from the inversion symmetry of the perovskite crystal structure. Due to the absorption in the bulk crystal, higher orders cannot be observed. Figure 1(c) shows the E dependences of the generation efficiencies of various harmonic orders obtained for $\theta = 0°$. As E increases, the behavior changes from perturbative, where the intensity obeys a scaling law (E^{2h}, h is an integer), to nonperturbative.

Figure 1(d) shows the circularly polarized HH emission spectra that were observed by excitation with left-handed circularly polarized (LCP) pulses with $E = 7\,\mathrm{MV/cm}$. The LCP and right-handed circularly polarized (RCP) components of the HHs were distinguished by using a $\lambda/4$ wave plate and a linear polarizer. The observed HHs mostly follow the selection rule of materials with fourfold symmetry, where harmonic orders equal to $(4 \times q + 1)$ (q is an integer) are LCP and those equal to $(4 \times q - 1)$ are RCP [35,36]. The observed circular polarization dependence reflects the symmetry of the perovskite structure, thus indicating a good crystallinity of our sample.

Because the generation mechanism of HHs in the sample is inherently related to the three-dimensional electronic structure of the material, we measured the orientation dependences of the HH intensities. Figure 2 shows the orientation dependences of the third-, fifth-, seventh-, and ninth-order harmonics obtained using linearly polarized MIR pulses, where the crystal orientation is defined by the relative angle θ between E and the Cl-Pb bond as defined in Fig. 1(a). The plots clearly show the fourfold rotation symmetry of the crystal. Moreover, the dips in the HH yield at 45°, 135°, 225°, and 315° (reflecting the anisotropy in the HH yield) become less apparent in the nonperturbative regime at higher-field strengths.

Due to the strong electronegativity of Cl, the Cl ions in $MAPbCl_3$ may attract electrons from Pb and the chemical bond may cause the strong directionality observed in Fig. 2. The attraction between the atoms also causes a hybridization

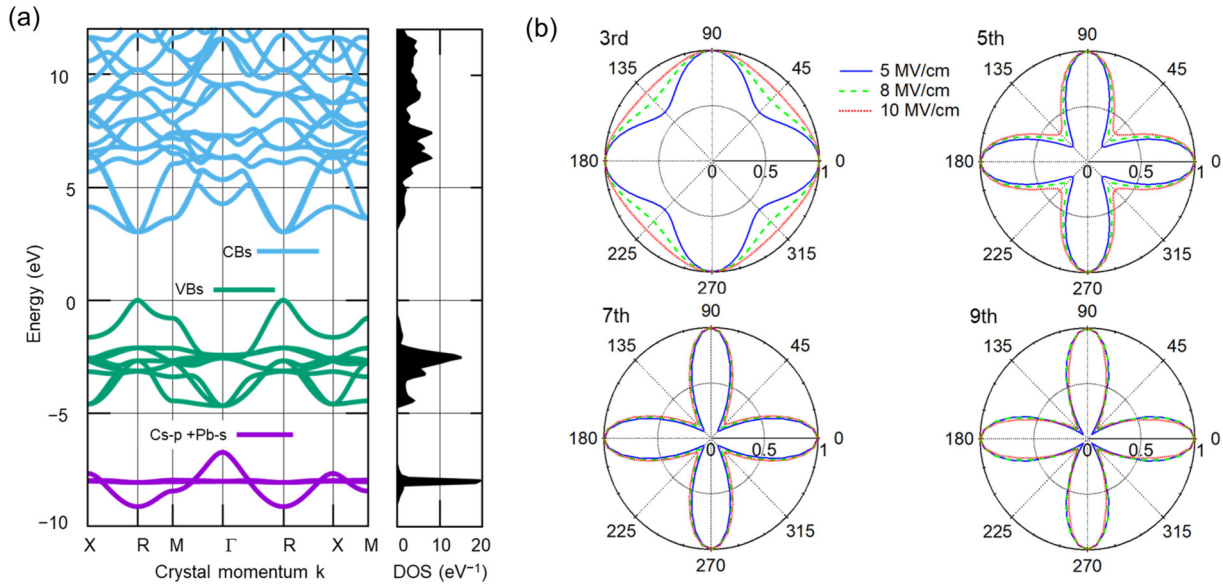

FIG. 3. (a) Electronic band structure and DOS for $CsPbCl_3$ calculated using first-principles DFT. (b) Calculated θ dependences of the HHG yield for $E = 5$, 8, and 10 MV/cm are shown with the blue, green, and red curves, respectively. The data for the third-, fifth-, seventh-, and ninth-order harmonics are provided and the data are normalized for clarity. The calculations shown are for an interband decoherence time $\tau = \infty$.

of the Pb s and Cl p orbitals, which are responsible for the antibonding character in the valence band maximum (VBM), whereas the conduction band has a nonbonding character [37,38]. Hence, to understand the HHG mechanism (which determines the observed complex crystal orientation dependence) in more detail, we considered the $MAPbCl_3$ band structure and its influence on the nonlinear current. The band structure and the density of states (DOS) were calculated using first-principles density functional theory (DFT) and the results are shown in Fig. 3(a). Here, we replaced the MA cation by a Cs cation (this is one of the best alternatives for simple calculations [39]). This approximation is justified [40], because the electronic contributions of the MA cation appear several electron volts below the Fermi level. Due to the resulting weak electronic interaction between the MA cation and the inorganic part of $MAPbCl_3$, the effect of the MA cation is negligible. The Cs contribution [Fig. 3(a), purple lines] also concentrates several electron volts below the Fermi level and is too deep to affect the HHG for field strengths on the order of 10 MV/cm.

The temporal evolution of the current density was calculated by using an *ab initio* quantum mechanical simulation based on the time-dependent density matrix (see SM Secs. III–IV [34,41–43]). Here, the HH spectra correspond to the modulus-squared Fourier transform of the time derivative of the calculated total current density $J_{\mathrm{total}}(t)$. The calculated crystal orientation dependences and their variation with the driving-field strength are shown in Fig. 3(b). We can confirm an excellent agreement with the experimentally observed data shown in Fig. 2. The calculated electric field dependence of the HH yield for $\theta = 0^\circ$ in Fig. 1(c) (solid lines) also well reproduces the experimental data (solid circles). Note that the total current density $J_{\mathrm{total}}(\omega)$ closely follows the intraband current of the nine uppermost valence bands (VBs), $J_{\mathrm{VBs}}(\omega)$ (SM Sec. V [34]).

To reveal the details of $J_{\mathrm{VBs}}(\omega)$, which comprises the contributions of the holes in the nine uppermost VBs [Fig. 3(a), green solid lines], we decompose it as follows,

$$J_{\mathrm{VBs}}(t) = -\frac{e}{\Omega m}\sum_{i\in\mathrm{VBs},\boldsymbol{k}}[n_{i,\boldsymbol{k}}(t) - n_{i,\boldsymbol{k}}(t=0)] \times \langle\varphi_{i,\boldsymbol{k}}^{(t)}|\hat{p} + \boldsymbol{A}(t)|\varphi_{i,\boldsymbol{k}}^{(t)}\rangle, \quad (1)$$

where m is the free-electron mass, e is the elementary charge, $\boldsymbol{A}(t)$ is the vector potential of the applied electric field $E(t)$ (in our case, due to the incident MIR pulse), $n_{i,\boldsymbol{k}}(t)$ is the transient population in the ith band at the initial wave vector $\boldsymbol{k}$, $|\varphi_{i,\boldsymbol{k}}^{(t)}\rangle$ are instantaneous eigenfunctions determined by the time-dependent Hamiltonian, and Ω is the volume of the unit cell. For the following discussion, we introduce the band-averaged population change in the nine uppermost VBs: $\Delta n_{\mathrm{VBs}}(t) = 1/\Omega\sum_{i\in\mathrm{VBs},\boldsymbol{k}}[n_{i,\boldsymbol{k}}(t) - n_{i,\boldsymbol{k}}(t=0)]$. The corresponding velocity can be obtained from the band-averaged intraband current of these VBs and the population using $J_{\mathrm{VBs}}(t) = e\Delta n_{\mathrm{VBs}}(t)V_{\mathrm{VBs}}(t)$. Here, we note that the single-particle expression of the transient population $n_{i,\boldsymbol{k}}(t)$ with the instantaneous one-body eigenstates $|\varphi_{i,\boldsymbol{k}}^{(t)}\rangle$ is straightforwardly derived with many-body eigenstates of the field-free Hamiltonian (SM Sec. IV [34]). Hence $n_{i,\boldsymbol{k}}(t)$ unambiguously describes the transient population in the bare bands.

It is important to elaborate the effects of the interband decoherence time on J_{total} and Δn_{VBs}, as such effects may cause real excited carriers in the valence and conduction bands [18]. We chose to approximate the decoherence by a simple homogeneous and time-independent decoherence time (such an approach can provide an excellent agreement in out-of-equilibrium experiments) [6,44–46]. Figure 4(a) shows the calculated total current J_{total} in the time domain for three different interband decoherence times τ ($= \infty$, 100 fs, 10 fs). It can be confirmed that $J_{\mathrm{total}}(t)$ hardly depends on τ.

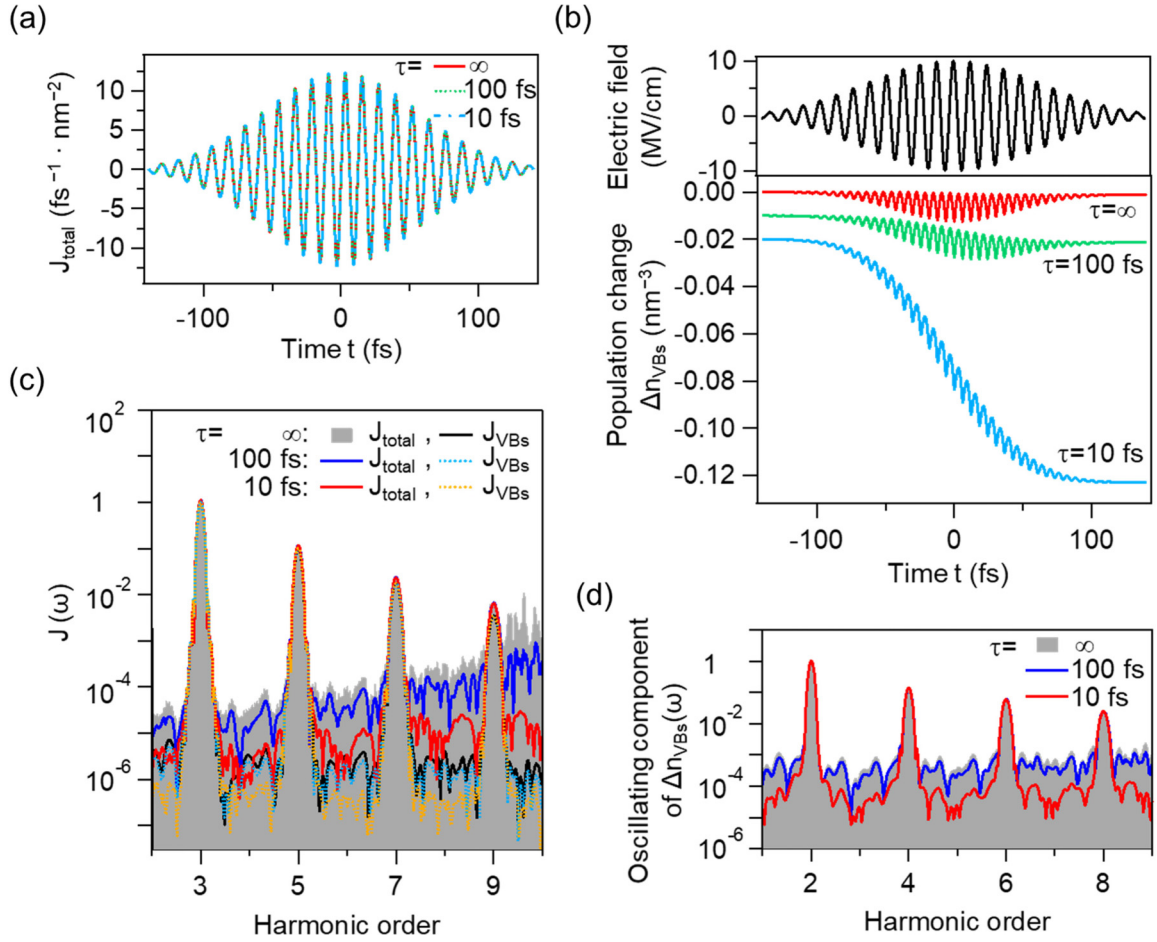

FIG. 4. (a) Calculated total current J_{total} and (b) population change Δn_{VBs} of the nine uppermost VBs in the time domain. Three data sets corresponding to three different interband decoherence times τ ($= \infty$, 100 fs, 10 fs) are provided. All calculations use a 10 MV/cm excitation pulse as shown in the upper panel of (b). (c) The spectra of J_{total} and J_{VBs} for the three τ values and (d) the spectra of the oscillating components in the population change Δn_{VBs}. Here, we analyzed the contribution of the virtual population change by subtracting the real population from the total population in the time domain shown in (b).

Furthermore, the HH components due to $J_{\text{total}}(\omega)$ are almost the same as those due to $J_{\text{VBs}}(\omega)$ [Fig. 4(c)]. To understand the contributions to J_{total}, the population change Δn_{VBs} in the nine uppermost VBs is provided in Fig. 4(b). The real population, which gradually increases and remains even after the excitation pulse has decayed, increases as τ becomes shorter. These facts indicate that the generated total current and the resultant HHG efficiency do not depend either on the decoherence time or on the real population. Moreover, the spectra $\Delta n_{\text{VBs}}(\omega)$ also do not change for different τ as shown in Fig. 4(d). Thus, it can be concluded that not the real population change but the virtual population change (SM Sec. VI [34]), which does not leave long-lived real excited carriers both in the real and momentum space of the crystal after passing the laser pulse out but appears as the oscillating component in the population change in Fig. 4(b) [22], constitutes the main source of current for HHG.

The above-mentioned decomposition, $J_{\text{VBs}}(t) = e\Delta n_{\text{VBs}}(t)V_{\text{VBs}}(t)$, allows us to assign the anisotropies of the HH yield to the nonlinearity of either Δn_{VBs} or V_{VBs}. The Fourier components of $J_{\text{VBs}}(t)$ can be described as $\text{FT}[\Delta n_{\text{VBs}}(t)\text{V}_{\text{VBs}}(t)](m\omega_0) = \sum_{l=-\infty}^{\infty} \Delta n_{\text{VBs}}^{(l)} \text{V}_{\text{VBs}}^{(m-l)}$. Here, $\Delta n_{\text{VBs}}^{(n)}$ and $V_{\text{VBs}}^{(n)}$ are the nth Fourier components of $\Delta n_{\text{VBs}}(t)$ and $V_{\text{VBs}}(t)$, respectively, and n, m, and l are integers. In Fig. 5(a) we plotted the calculated $J_{\text{VBs}}(\omega)$ for two different crystal orientations. Only the even components $\Delta n_{\text{VBs}}^{(2l)}$ in Fig. 5(b) and the odd components $V_{\text{VBs}}^{(2l+1)}$ in Fig. 5(c) contribute to the current because of the sample's inversion symmetry and sign-independent excitation, $V_{\text{VBs}}[-E(t)] = -V_{\text{VBs}}[E(t)]$ and $\Delta n_{\text{VBs}}[-E(t)] = \Delta n_{\text{VBs}}[E(t)]$. Thus, the frequency components $J_{\text{VBs}}^{(2m+1)}$(only odd orders), derived by summation of the products of the Fourier components ($\Delta n_{\text{VBs}}^{(n)}$ and $V_{\text{VBs}}^{(n)}$), constitute the effective source of HHG. Figure 5(d) compares the ratios of $J_{\text{VBs}}(\omega)$, $\Delta n_{\text{VBs}}(\omega)$, and $V_{\text{VBs}}(\omega)$ calculated for $\theta = 0^\circ$ to those for $\theta = 45^\circ$. The ratios of J_{VBs} and Δn_{VBs} shown in red and blue, respectively, exhibit a similar increase with harmonic order. In contrast, the ratio of $V_{\text{VBs}}(\omega)$ stays rather constant (even the features for weaker electric fields of 1 MV/cm are similar). These results clearly indicate that the anisotropy of the HH yield can be attributed to the anisotropic nonlinearity of the population change,

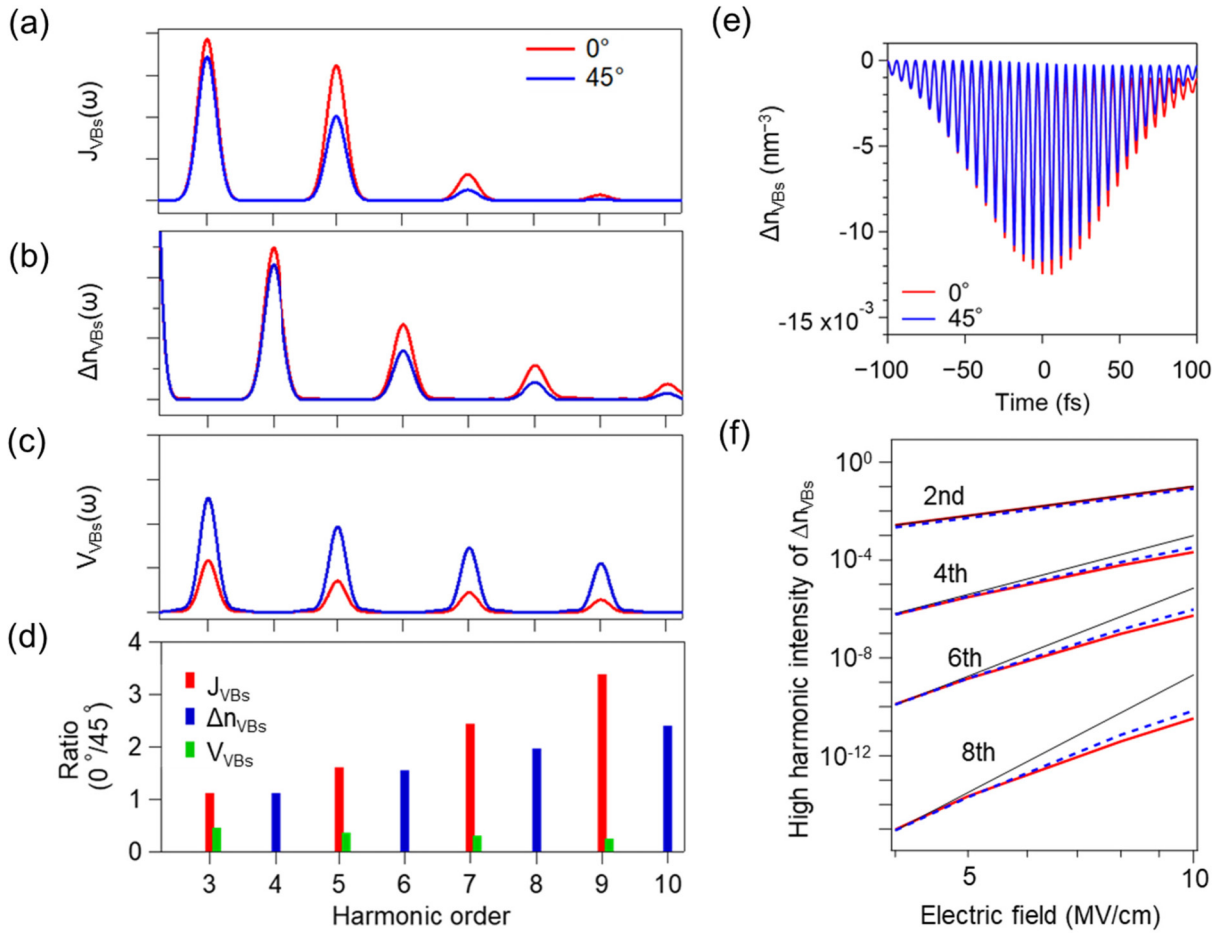

FIG. 5. (a)–(c) Fourier spectra of current, population change, and velocity averaged over the nine uppermost VBs in the time domain, $J_{\mathrm{VBs}}(\omega)$, $\Delta n_{\mathrm{VBs}}(\omega)$, and $V_{\mathrm{VBs}}(\omega)$, for $E = 10\,\mathrm{MV/cm}$. (d) Comparison of the harmonic intensity ratios of $J_{\mathrm{VBs}}(\omega)$, $\Delta n_{\mathrm{VBs}}(\omega)$, and $V_{\mathrm{VBs}}(\omega)$ for $\theta = 0^\circ$ to those for $\theta = 45^\circ$. The three types of ratios are shown with the red, blue, and green bars, respectively. (e) Calculated population changes $\Delta n_{\mathrm{VBs}}(t)$ for $\theta = 0^\circ$ [these data are the same as those shown in Fig. 4(b) for $\tau = \infty$] and 45° are shown with the red and blue curves, respectively. (f) Electric field dependences of the calculated $\Delta n_{\mathrm{VBs}}(\omega)$ for the second, fourth, sixth, and eighth order for $\theta = 0^\circ$ (red solid curves) and $\theta = 45^\circ$ (blue dashed curves). The black lines are proportional to E^{2h} and serve as guides for the eye. The data are offset for clarity.

rather than to the anharmonic potential causing high-order components of $V_{\mathrm{VBs}}(\omega)$.

Thus, the field dependences of the HHG orientation dependence can be related to the field dependence of the virtual population $\Delta n_{\mathrm{VBs}}(t)$. Figure 5(e) plots the calculated $\Delta n_{\mathrm{VBs}}(t)$ for the cases of $\theta = 0^\circ$ (red curve) and 45° (blue curve). Figure 5(f) shows the field dependences of the even components $\Delta n^{(2l)}_{\mathrm{VBM}}$ for $\theta = 0^\circ$ (red solid curves) and 45° (blue dashed curves), which are the Fourier components of $\Delta n_{\mathrm{VBs}}(t)$. The second harmonics of $\Delta n^{(n)}_{\mathrm{VBs}}$ for both cases closely follow a second-order power law, reflecting that the virtual population in the time domain [Fig. 5(e)] closely follows the absolute value of the electric field and that the population change shows no significant directionality. On the other hand, the higher nonlinear components ($2h = 4, 6, 8$) show a directionality in the field dependence. The field dependences of $\Delta n^{(2h)}_{\mathrm{VBs}}$ of these higher orders in Fig. 5(f) deviate from the power law E^{2h} and those for $\theta = 0^\circ$ saturate earlier than those for $\theta = 45^\circ$. This calculation result implies that a more efficient transfer of virtual population from VB to conduction band occurs along the Cl-Pb bond direction ($\theta = 0^\circ$). As the electric field increases, the initially lower HH yield along $\theta = 45^\circ$ catches up with that along 0° and the anisotropic behavior becomes less apparent. The increase of the ratio of $\Delta n_{\mathrm{VBs}}(\omega)$ with increasing order shown in Fig. 5(d) can be qualitatively explained by evaluating the angle dependence of the virtual population change Δn_{VBs} (SM Sec. VII [34]).

In conclusion, we have presented data on the anisotropy in the crystal orientation dependence of the HH yield for a halide perovskite single crystal. We have shown that the degree of anisotropy in the orientation dependence is a function of the applied electric field strength and that it can be well reproduced by an *ab initio* approach in the time domain. Our microscopic analysis of the intraband current indicates that the dynamics of the virtual population are responsible for the orientation dependence of HHG in the nonperturbative regime. Our results emphasize that the virtual population is another important factor for HHG besides the motion of accelerated carriers in solids.

This study was supported by JSPS KAKENHI (Grants No. 19H05465, No. 18K14145, No. 18H05250, and No. 19H02623), JST CREST (Grants No. JPMJCR15N1 and No. JPMJCR16N3), JST COI (Grant No. JPMJCE1313), MEXT Q-LEAP (Grants No. JPMXS0118067246 and No. JPMXS0118068681), and the Exploratory Challenge on Post-K Computer from MEXT. The computation in this work was done using the facilities of the Supercomputer Center of the Institute for Solid State Physics, The University of Tokyo, and the K computer provided by the RIKEN Advanced Institute for Computational Science through the HPCI System Research project (Project ID: hp180174).

[1] S. Y. Kruchinin, F. Krausz, and V. S. Yakovlev, Rev. Mod. Phys. **90**, 021002 (2018).
[2] P. B. Corkum and F. Krausz, Nat. Phys. **3**, 381 (2007).
[3] W. Kuehn, P. Gaal, K. Reimann, M. Woerner, T. Elsaesser, and R. Hey, Phys. Rev. Lett. **104**, 146602 (2010).
[4] S. Ghimire, A. D. DiChiara, E. Sistrunk, P. Agostini, L. F. DiMauro, and D. A. Reis, Nat. Phys. **7**, 138 (2011).
[5] O. Schubert, M. Hohenleutner, F. Langer, B. Urbanek, C. Lange, U. Huttner, D. Golde, T. Meier, M. Kira, S. W. Koch, and R. Huber, Nat. Photonics **8**, 119 (2014).
[6] T. T. Luu, M. Garg, S. Y. Kruchinin, A. Moulet, M. T. Hassan, and E. Goulielmakis, Nature (London) **521**, 498 (2015).
[7] M. Garg, M. Zhan, T. T. Luu, H. Lakhotia, T. Klostermann, A. Guggenmos, and E. Goulielmakis, Nature (London) **538**, 359 (2016).
[8] G. Vampa, T. J. Hammond, N. Thiré, B. E. Schmidt, F. Légaré, C. R. McDonald, T. Brabec, and P. B. Corkum, Nature (London) **522**, 462 (2015).
[9] M. Hohenleutner, F. Langer, O. Schubert, M. Knorr, U. Huttner, S. W. Koch, M. Kira, and R. Huber, Nature (London) **523**, 572 (2015).
[10] G. Ndabashimiye, S. Ghimire, M. Wu, D. A. Browne, K. J. Schafer, M. B. Gaarde, and D. A. Reis, Nature (London) **534**, 520 (2016).
[11] D. Golde, T. Meier, and S. W. Koch, Phys. Rev. B **77**, 075330 (2008).
[12] Y. Sanari, T. Otobe, Y. Kanemitsu, and H. Hirori, Nat. Commun. **11**, 3069 (2020).
[13] K. Kaneshima, Y. Shinohara, K. Takeuchi, N. Ishii, K. Imasaka, T. Kaji, S. Ashihara, K. L. Ishikawa, and J. Itatani, Phys. Rev. Lett. **120**, 243903 (2018).
[14] Y. S. You, D. A. Reis, and S. Ghimire, Nat. Phys. **13**, 345 (2017).
[15] H. Liu, Y. Li, Y. S. You, S. Ghimire, T. F. Heinz, and D. A. Reis, Nat. Phys. **13**, 262 (2017).
[16] S. T. Cundiff, A. Knorr, J. Feldmann, S. W. Koch, E. O. Göbel, and H. Nickel, Phys. Rev. Lett. **73**, 1178 (1994).
[17] O. D. Mücke, T. Tritschler, M. Wegener, U. Morgner, and F. X. Kärtner, Phys. Rev. Lett. **89**, 127401 (2002).
[18] W. Kuehn, P. Gaal, K. Reimann, M. Woerner, T. Elsaesser, and R. Hey, Phys. Rev. B **82**, 075204 (2010).
[19] F. Junginger, B. Mayer, C. Schmidt, O. Schubert, S. Mährlein, A. Leitenstorfer, R. Huber, and A. Pashkin, Phys. Rev. Lett. **109**, 147403 (2012).
[20] E. Yablonovitch, J. P. Heritage, D. E. Aspnes, and Y. Yafet, Phys. Rev. Lett. **63**, 976 (1989).
[21] Y. Shinohara, K. Yabana, Y. Kawashita, J.-I. Iwata, T. Otobe, and G. F. Bertsch, Phys. Rev. B **82**, 155110 (2010).
[22] A. Sommer, E. M. Bothschafter, S. A. Sato, C. Jakubeit, T. Latka, O. Razskazovskaya, H. Fattahi, M. Jobst, W. Schweinberger, V. Shirvanyan, V. S. Yakovlev, R. Kienberger, K. Yabana, N. Karpowicz, M. Schultze, and F. Krausz, Nature (London) **534**, 86 (2016).
[23] P. Jürgens, B. Liewehr, B. Kruse, C. Peltz, D. Engel, A. Husakou, T. Witting, M. Ivanov, M. J. J. Vrakking, T. Fennel, and A. Mermillod-Blondin, arXiv:1905.05126.
[24] T. Handa, H. Tahara, T. Aharen, and Y. Kanemitsu, Sci. Adv. **5**, eaax0786 (2019).
[25] T. Yamada, T. Aharen, and Y. Kanemitsu, Phys. Rev. Lett. **120**, 057404 (2018).
[26] Y. Kanemitsu and T. Handa, Jpn. J. Appl. Phys. **57**, 090101 (2018).
[27] A. Kojima, K. Teshima, Y. Shirai, and T. Miyasaka, J. Am. Chem. Soc. **131**, 6050 (2009).
[28] M. Saliba, T. Matsui, K. Domanski, J.-Y. Seo, A. Ummadisingu, S. M. Zakeeruddin, J.-P. Correa-Baena, W. R. Tress, A. Abate, A. Hagfeldt, and M. Grätzel, Science **354**, 206 (2016).
[29] Z.-K. Tan, R. S. Moghaddam, M. L. Lai, P. Docampo, R. Higler, F. Deschler, M. Price, A. Sadhanala, L. M. Pazos, D. Credgington, F. Hanusch, T. Bein, H. J. Snaith, and R. H. Friend, Nat. Nanotechnol. **9**, 687 (2014).
[30] G. Xing, N. Mathews, S. S. Lim, N. Yantara, X. Liu, D. Sabba, M. Grätzel, S. Mhaisalkar, and T. C. Sum, Nat. Mater. **13**, 476 (2014).
[31] F. P. García de Arquer, A. Armin, P. Meredith, and E. H. Sargent, Nat. Rev. Mater. **2**, 16100 (2017).
[32] H. Hirori, P. Xia, Y. Shinohara, T. Otobe, Y. Sanari, H. Tahara, N. Ishii, J. Itatani, K. L. Ishikawa, T. Aharen, M. Ozaki, A. Wakamiya, and Y. Kanemitsu, APL Mater. **7**, 041107 (2019).
[33] K. Ohara, T. Yamada, H. Tahara, T. Aharen, H. Hirori, H. Suzuura, and Y. Kanemitsu, Phys. Rev. Mater. **3**, 111601(R) (2019).
[34] See Supplemental Material at http://link.aps.org/supplemental/10.1103/PhysRevB.102.041125 for the details of sample preparation and experimental methods (Secs. I and II), details of the theoretical calculation (Secs. III and IV) and the calculated HH spectra (Sec. V), explanation of the virtual population change in terms of the Rabi flopping (Sec. VI), and an explanation of the dependence of the anisotropic population on the harmonic (Sec. VII), which includes Refs. [41–43].
[35] C. L. Tang and H. Rabin, Phys. Rev. B **3**, 4025 (1971).
[36] N. Tancogne-Dejean, O. D. Mücke, F. X. Kärtner, and A. Rubio, Nat. Commun. **8**, 745 (2017).
[37] T. Umebayashi, K. Asai, T. Kondo, and A. Nakao, Phys. Rev. B **67**, 155405 (2003).

[38] J. Even, L. Pedesseau, J.-M. Jancu, and C. Katan, J. Phys. Chem. Lett. **4**, 2999 (2013).
[39] G. Murtaza and I. Ahmad, Physica B **406**, 3222 (2011).
[40] S. X. Tao, I. Schmidt, G. Brocks, J. K. Jiang, I. Tranca, K. Meerholz, and S. Olthof, Nat. Commun. **10**, 2560 (2019).
[41] P. Hohenber and W. Kohn, Phys. Rev. **136**, B864 (1964).
[42] J. P. Perdew and Y. Wang, Phys. Rev. B **45**, 13244 (1992).
[43] Chr. Kn. Møller, Nature (London) **182**, 1436 (1958).
[44] T. Meier, G. von Plessen, P. Thomas, and S. W. Koch, Phys. Rev. Lett. **73**, 902 (1994).
[45] N. Yoshikawa, T. Tamaya, and K. Tanaka, Science **356**, 736 (2017).
[46] S. A. Sato, J. W. McIver, M. Nuske, P. Tang, G. Jotzu, B. Schulte, H. Hübener, U. De Giovannini, L. Mathey, M. A. Sentef, A. Cavalleri, and A. Rubio, Phys. Rev. B **99**, 214302 (2019).